Volume 18
Number 2

December *2016*
(ISSN 1109-1606)

Journal of APPLIED ELECTROMAGNETISM

JAE

Institute of Communication and Computer Systems

Athens - GREECE

Volume 18 December 2016
Number 2 (ISSN 1109-1606)

JOURNAL
OF
APPLIED ELECTROMAGNETISM

Trans Black Sea Region Union of Applied Electromagnetism

BSUAE

Institute of Communication and Computer Systems

Athens - GREECE

Volume 18 **Number 2**

December 2016

TRANS BLACK SEA REGION UNION OF APPLIED ELECTROMAGNETISM (BSUAE)

JOURNAL OF APPLIED ELECTROMAGNETISM

Institute of Communication and Computer Systems

Athens - GREECE

Editor: Panayiotis Frangos (Greece), pfrangos@central.ntua.gr

Honorary Editor: Nikolaos K. Uzunoglu (Greece), nuzu@central.ntua.gr

Board of Associate Editors

D. Dimitrov (Bulgaria), dcd@tu-sofia.bg
V. Dumbrava (Lithuania), vydum@ktu.lt
G. Georgiev (Bulgaria), gngeorgiev@yahoo.com
G. Matsopoulos (Greece), gmatso@esd.ece.ntua.gr

Editorial Board

ALBANIA
G. Bardhyf, bardhylgolemi@live.com
C. Pirro, p_cipo@yahoo.com

ARMENIA
H. Bagdasarian, hovik@seua.sci.am
H. Terzian, hterzian@seua.sci.am

BULGARIA
A. Antonov, asantonov@abv.bg
A. Lazarov, lazarov@bfu.bg
S. Savov, savovsv@yahoo.com

GEORGIA
R. Zaridze, rzaridze@laetsu.org

GERMANY
M. Georgieva – Grosse, mariana.georgieva-grosse@de.bosch.com

GREECE
H. Anastassiu, ANASTASIOU.Christos@haicorp.com
I. Avramopoulos, hav@mail.ntua.gr
G. Fikioris, gfiki@cc.ece.ntua.gr
J. Kanellopoulos, ikanell@cc.ece.ntua.gr
G. Karagiannidis, geokarag@auth.gr
G. Kliros, gsksma@hol.gr
T. Mathiopoulos, mathio@space.noa.gr
C. Moschovitis, harism@noc.ntua.gr
K. Nikita, knikita@cc.ece.ntua.gr

I. Ouranos, iouranos@central.ntua.gr
E. Papkelis, spapkel@central.ntua.gr
J. Sahalos, sahalos@auth.gr
M. Theologou, theolog@cs.ntua.gr
N. Triantafyllou, nitriant@central.ntua.gr
K. Ksystra, katksy@central.ntua.gr
A. Malamou, annamalamou@yahoo.gr
S. Bourgiotis, sbourgiotis@mail.ntua.gr

JORDAN
N. Dib, nihad@just.edu.jo

KAZAKSHTAN
S. Sautbekov, sautbek@mail.ru

LITHUANIA
L. Svilainis, linas.svilainis@ktu.lt

RUSSIA
M. Bakunov, bakunov@rf.unn.ru
A. Grigoriev, adgrigoriev@mail.ru

SERBIA
B. Reljin, ereljin@ubbg.etf.bg.ac.yu

SPAIN
E. Gago – Ribas, egr@tsc.uniovi.es
M. Gonzalez – Morales, gonmor@yllera.tel.uva.es

UNITED KINGDOM
G. Goussetis, G.Goussetis@hw.ac.uk

Publishing Department

N. Triantafyllou, nitriant@central.ntua.gr
K. Ksystra, katksy@central.ntua.gr
A. Malamou, annamalamou@yahoo.gr
S. Bourgiotis, sbourgiotis@mail.ntua.gr

Journal of Applied Electromagnetism

Copyright Form

The undersigned I confirm that I agree the publication of the article

in the Journal of Applied Electromagnetism and the copyright to belong to Trans Black Sea Union of Applied Electromagnetism. I understand that I have the full right to reuse this manuscript for my own purposes.

Name:

Surname:

Address:

E-mail:

Signed:

***Please send the previous form signed either by e-mail to pfrangos@central.ntua.gr , or by fax to the fax number: +30 210 772 2281, attention of Prof. P. Frangos.**

Address

Institute of Communication and Computer Systems,

National Technical University of Athens,

9, Iroon Polytechniou Str.,

157 73 Athens - GREECE

Tel: (+30) 210 772 3694

Fax: (+30) 210 772 2281, attention of Prof. P. Frangos

e-mail: pfrangos@central.ntua.gr

Web site: **http://jae.ece.ntua.gr**

TRANS BLACK SEA REGION UNION OF APPLIED ELECTROMAGNETISM (BSUAE)

JOURNAL OF APPLIED ELECTROMAGNETISM (JAE)

Volume 18 Number 2 December 2016

CONTENTS

INDOOR PROPAGATION SHADOWING MODEL FOR WIRELESS SENSOR NETWORKS

Z. Ganev, S. Savov 1

Our radio propagation model is derived on a combination of analytical and empirical methods. The empirical approach is based on "curve-fitting" method applied to measured data. All propagation factors are taken into consideration, both known and unknown, through actual power measurements. However, the validity of an empirical model at certain frequency or environment, can only be established by proper measurements.

SOLUTIONS OF THE EQUATION OF MOTION OF POISEUILLE'S LAMINAR FLOW FOR A MAGNETIC FLUID (short paper)

K. Kotetishvili, N. Kobalia, G. Chikhladze 9

The paper deals with reception of solutions for the equation of motion of Poiseuille's laminar flow in magnetic fluids. The different behavior of the magnetic fluid placed into the rotating magnetic field is evident and clear. Here additionally the strong field of the direct, constant current is applied, associated with the growth, and considering the motion of the fluid in the area. The rotating effect of nano-particles in the transversal magnetic field is considered. In MRI of sick fields it represents rather big changes.

ON A VISUALIZATION OF LOW FREQUENCY MAGNETIC FIELDS IN MAGNETOTHERAPY (selected from CEMA'15 Conference)

B. Kudrin, V. Nikolov 14

In this work we describe a process of visualization of low-frequency magnetic field generated by several coils. The technic was applied to visualize the magnetic field occurring in a special magnetotherapy device — magneto bed. The obtained image shows a patient position, coils, and the magnetic field distribution in the area of coils action. To do this we use 'Paraview' tools, body model and the special scenario – 'Python' language script.

EMG DRIVEN ACTIVE PROSTHESIS: SIGNAL ACQUISITION SYSTEM DESIGN AND INITIAL EXPERIMENTAL STUDY (selected from CEMA'15 Conference)

D. Dimitrov, V. A. Nedialkov, K. Dimitrov **23**

A multi-channel EMG amplifier and acquisition system is proposed. The system is composed of portable signal amplifier and dedicated real-time signal processing software. The system is intended to be used with myoelectric prostheses, therefore there is an emphasis on the multichannel real-time acquisition, portability, current consumption and connectivity features. The goal of the design is to implement the latest low-power high speed technologies available on the market today and also the system is intended to test EMG signal processing algorithms. This document covers the EMG signal all the way from the muscle through the amplifier, the Driven Right Leg (DRL) noise suppressor, filtering, digitalization, PC communication, the signal processing algorithm and the real-time visualization of the results. The article includes complete schematics, analysis and tests of the device.

INDOOR PROPAGATION SHADOWING MODEL FOR WIRELESS SENSOR NETWORKS

Z. Ganev, S. Savov

Department of Electrical Engineering, Technical University of Varna,
9010 Varna, Bulgaria
Email: zganev@gmail.com, Email: sava.savov12@gmail.com

Abstract

Our radio propagation model is derived on a combination of analytical and empirical methods. The empirical approach is based on "curve-fitting" method applied to measured data. All propagation factors are taken into consideration, both known and unknown, through actual power measurements. However, the validity of an empirical model at certain frequency or environment, can only be established by proper measurements.

1. INTRODUCTION

In this paper two cases of propagation are considered: a) two- floor propagation and b) three-floor propagation in one office building. Additional losses are caused by radio waves going through ceilings and reflections and diffractions from walls and edges.

Our radio propagation model is derived on a combination of analytical and empirical methods. The empirical approach is based on "curve-fitting" method applied to measured data. All propagation factors are taken into consideration, both known and unknown, through actual power measurements. However, the validity of an empirical model at certain frequency or environment, can only be established by proper measurements.

"Log-normal shadowing model" is used here for predicting large-scale coverage for wireless sensor networks (WSN). Applying this model helps one to estimate the energy capacity of WSN before such systems to be deployed.

In our work first, we calculate path loss exponent (n) and then standard deviation (σ), assuming Gaussian noise in the channel. Second, we estimate the received

power (Pr) at given distance (d) and predict the likelihood that the received signal level at this distance will be greater than given threshold γ: Pr[Pr(d) > γ]. Finally, we find out the percentage U(γ) of the area with a radius d, where received signal will be greater than a certain threshold γ.

2. PROPAGATION MODEL

This is an empirical model that try to approximate analytically the results of measurement. The path-loss function of the distance can be represented in the following form [1 - 6]

$$\mathrm{PL(d)} = \mathrm{PL(d_0)(d/d_0)^n} \tag{1}$$

or in logarithmic form [4 - 6]

$$PL_{dB}(d) = PL_{dBm}(d_0) + 10n\lg(d/d_0) + X_\sigma \tag{2}$$

where (d) is the distance, (d0) is the reference distance, and (X_σ) is a Gaussian noise power (in dBm). Here MMSE (minimum mean square error) estimation about the path-loss exponent (n) is applied and the standard deviation (σ) is found.

The reference distance for indoor propagation model usually is assumed to be d0=1m and the path loss there in our case is assumed to be $PL(d_0) = -32dBm$. The sum of squared errors that should be minimized is [6]

$$\mathrm{S(n)} = \sum_{k=0}^{N} \left(\mathrm{p_k} - \mathrm{q_k n}\right)^2 \tag{3}$$

where new coefficients

$$\mathrm{q_k} = -10\lg(\mathrm{d_k}/\mathrm{d_0}) \tag{4}$$

and

$$\mathrm{p_0} = 0,\ \mathrm{p_k} = -\mathrm{p(d_k)} + \mathrm{p_0} \tag{5}$$

are introduced. For the MMSE algorithm S(n) is found by the following simple quadratic expression

$$S(n) = A - 2Bn + Cn^2 \tag{6}$$

with new defined coefficients

$$A = \sum_{k=0}^{N} p_k^2 \; ; \quad B = \sum_{k=0}^{N} p_k q_k \; ; \quad C = \sum_{k=0}^{N} q_k^2 \tag{7}$$

(k=1,2,…,N). Here N is the *total number of the measurements*, while (k=0) is related to the reference point. The *necessary condition for minimum*

$$\frac{dS}{dn} = 0 \tag{8}$$

leads to the following equation for the path-loss exponent n

$$n = B / C \tag{9}$$

It can be shown that an appropriate expression for the *standard deviation* is

$$\sigma[dB] = \sqrt{S(n) / N} \tag{10}$$

In general, a greater number of measurements are needed to reduce σ.

3. RESULTS FROM SIMULATIONS

3.1. Calculation of the path loss exponent (n) and the standard deviation (σ) using measured results

Here we presented two different best fit lines [10]:

a) "the two-floor results" of measurements (with circles);
b) "the three-floor results" of measurements (with squares).

The range of measurements is: d = [10–34m]. In these experiments the carrier frequency is f = 914 MHz. Both best fit lines (with linear regressions) are shown by dashed lines in Fig.1. More accurate results for the parameters of both linear regression lines are:

a) (two-floor) $n_1 = 5.32$; $\sigma_1 = 3.76$ dB;
b) (three-floor) $n_2=5.52$; $\sigma_2 = 4.36$ dB.

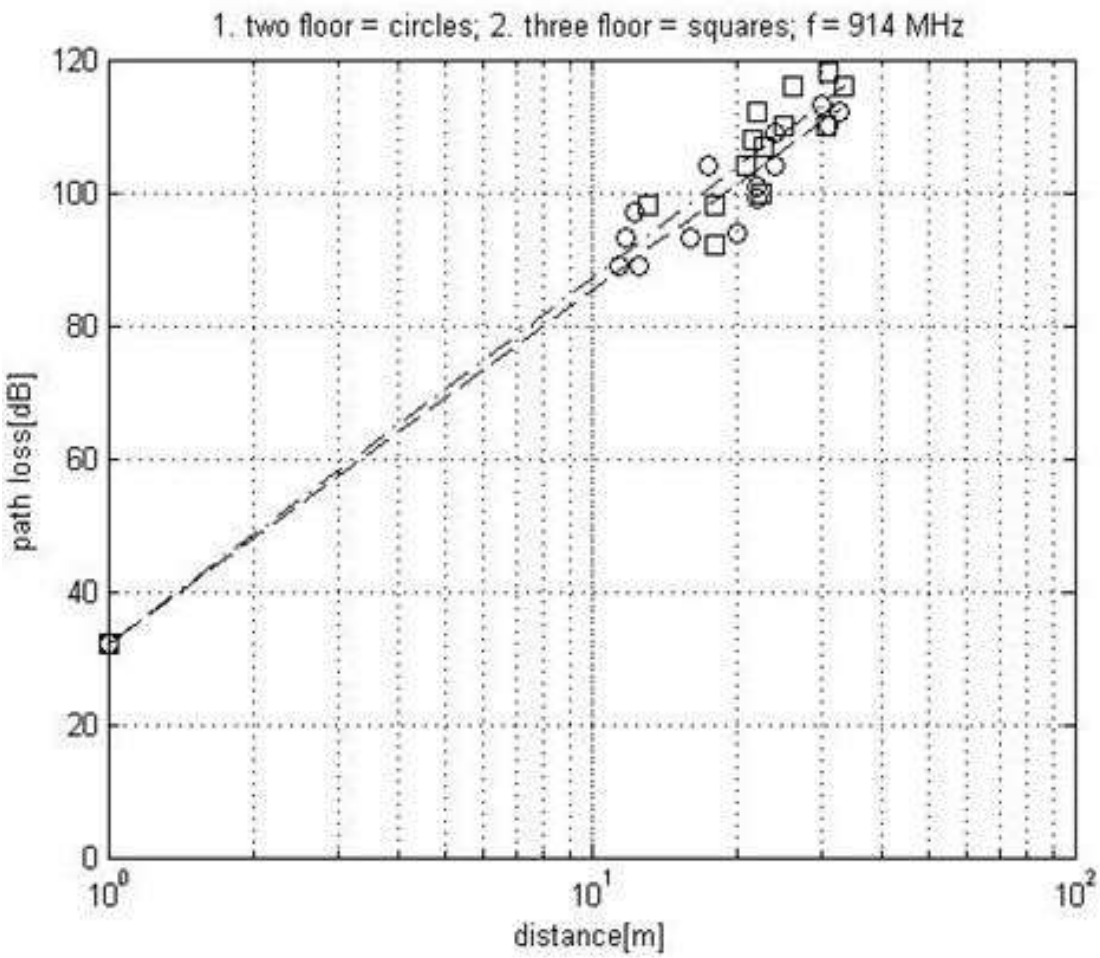

Fig. 1. Best fit linear regressions.

We observe one interesting and expected result from these simulations: the power parameter (n) for the case of "three-floor" is higher than the same parameter for the case of "two-floor". This event can be explained by additional "*through-ceiling propagation*".

3.2. Statistical data processing of the obtained results

a) two-floor case at distance d=32m

a1) <u>estimation of the received power</u> (at d=32m)

It is given by the following equation

$$P_r(d)= -32\text{dBm} - 10\, n_1 \lg(d/d_0) \qquad (11)$$

It can be found for this distance the following power

$$P_r(d = 32m) = -32dBm - 10(5.32)\lg(32/1) = -112.1 \text{ dBm}$$

A Gaussian random variable having zero mean and standard deviation σ_1 = 3.76 dB could be added to this value to simulate random shadowing effects at *d*=32m.

a2) <u>likelihood prediction of the received signal to be greater than the level γ</u> (here γ = - 116 dBm).

The probability that the received signal level will be greater than γ= -116 dBm is given by the following equation [5]

$$\Pr[P_r(d) > \gamma] = Q\left(\frac{\gamma - \Pr(d)}{\sigma 1}\right) = Q(-1.04) = 0.85 = 85\% \quad (12)$$

where new auxiliary function (for argument z < 0) is involved [5]

$$Q(z)=0.5[1 + \text{erf}\,(z/\sqrt{2})] \quad (13)$$

and erf(x) is the "error function" (this special function is available in Matlab).

a3) <u>percentage prediction of the area within a d=32 m radius</u> (that receives signals with a level greater than " γ ").

The probability that the received signal level will be greater than γ= -116dBm is presented by the following equation [5]

$$U(\gamma)=0.5\{1+\exp(1/b^2)[1-\text{erf}(1/b)]\} \quad (14)$$

where erf(x) is already defined function above and the new parameter here is

$$b=(10\, n_1.\lg e)/(\sigma_1.\sqrt{2}) = 4.345 \quad (15)$$

The value obtained by (14) is U(-116) = 89% (of the area that receives coverage above – 116 dBm) .

b) three-floor case at distance d=32m

Similar analysis is performed here.

b1) <u>estimation of the received power</u> (at d=32m). It is given by (11)

$$P_r(d) = -32dBm - 10\, n_2 lg(d/d_0)$$

It can be found for this distance the following power

$$P_r(d = 32m) = -32dBm - 10(5.52)lg(32/1) = -115.1\ dBm$$

A Gaussian random variable having zero mean and standard deviation σ2 = 4.36 dB could be added to this value to simulate random shadowing effects at *d*=32m.

b2) likelihood prediction of the received signal- to be greater than the level "γ" (here γ = - 116 dBm).

The probability that the received signal level will be greater than γ= -116 dBm is given by (12)

$$Pr[P_r(d) > \gamma] = Q\left(\frac{\gamma - Pr(d)}{\sigma 2}\right) = Q(-0.9) = 0.818 = 81.8\%$$

where the function Q(z) is defined by (13).

b3) percentage prediction of the area within a d=32 m radius (that receives signals with a level greater than " γ ").

The probability that the received signal level will be greater than γ= -116 dBm is found by equations (14) and (15).

Here,

$$b = (10\, n_2 . lge)/(\sigma_2 . \sqrt{2}) = 3.9$$

and for the percentage is obtained the following value U = 74.2 % .

4. CONCLUSION

Our "best-fit model" (with linear regression) could be applied to variety of scenarios in the area of WSN. We can apply this model in different kind of environments, with different carrier frequencies and distances.

The log-normal distribution describes the random shadowing effects which occur over a large number of measurement locations which have the same T-R (transmitter – receiver) separation, but have different levels of clutter on the propagation

path. This phe¬nomenon is referred to as “log-normal shadowing model”. This model implies that measured signal levels at a specific T-R separation have a Gaussian (normal) distribution about the distance-dependent mean, where the measured signal levels (received power) have values in dBm units. The standard devia¬tion of the Gaussian distribution that describes the shadowing has units in dB. Thus, the random effects of shadowing are easily accounted for the case of Gaussian distribution.

The closed reference distance d0, the path-loss at this distance PL(d0), the path-loss exponent n, and the stan¬dard deviation σ, statistically describe the path-loss model for an arbitrary loca¬tion having a specific T-R separation, and this model may be used in computer simulation to provide received power levels for random locations in communica¬tion system design and analysis.

In practice, the values of n and σ are computed from measured data (as described above), using linear regression, such that the difference between the measured and estimated path losses is minimized in a mean square error sense (MMSE method) over a wide range of mea¬surement locations and T-R separations.

In our case is visible that the path loss constant (parameter n) is bigger for the case in ,,three-floor" than the case in ,,two- floor" example. This can be explained by the additional shadowing effects for the ,,three-floor" example.

ACKNOWLEDGMENT

This study is supported by Shota Rustaveli National Science Foundation grant #30/09.

REFERENCES

[1] H.Karl.,A.Willig, “Protocols and architectures for wireless sensor networks”, John Wiley & Sons, 2005.

[2] Azar, Y., Wong, G. N., Wang, K., Mayzus, R., Schulz, J. K., Zhao, H., Gutierrez, F., Hwang, D., Rappaport, T. S., “28 GHz Propagation Measurements for Outdoor Cellular Communications Using Steerable Beam Antennas in New York City”, to appear in the 2013 IEEE International Conference on Communications (ICC), Jun 9-13, 2013.

[3] Alejandro Martŕnez-Sala, Jose-Marŕa Molina-Garcia-Pardo, Esteban Egea-Lŕopez, Javier Vales-Alonso,Leandro Juan-Llacer, and Joan Garcŕa-Haro, "An Accurate Radio Channel Model forWireless Sensor Networks Simulation", Journal of communications and networks, vol7, No4, Dec 2005.

[4] Claude Oestges, "Propagation Modeling for Wireless Sensor Networks", Report, Catholique Universite de Louvain, 2005.

[5] T. Rappaport., "Wireless Communications (Principles and Practice)", 2nd ed., Prentice Hall, 2002.

[6] S.Savov, Z.Ganev, "Indoor Propagation Path Loss Modeling for Wireless Sensor Networks", ICEST Nis, Serbia., Jun 2014.

[7] D. Janvier, "Propagation Models for Wireless Sensor Communications", Report, Catholique Universite de Louvain, 2006.

[8] T. Rappaport et al., "State of the Art in 60 GHz Integrated Circuits and Systems for Wireless Communications", Proc. IEEE, no. 8, 2011, pp. 1390 – 1436.

[9] Rappaport et. al., "Millimeter wave mobile communications for 5 G : it will work ! ", IEEE Access, May 2013.

[10] Ganev Z., Savov S., ,,Log-normal shadowing model for Wireless Sensor Networks", CEMA2014, 16-18/10/2014, Conference Proceedings, pp.61-64, Sofia,Bulgaria.

SOLUTIONS OF THE EQUATION OF MOTION OF POISEUILLE'S LAMINAR FLOW FOR A MAGNETIC FLUID

(short paper)

K.V. Kotetishvili, N. Kobalia, G.G. Chikhladze

Georgian Technical University, 0175, 77, M. Kostava str., Tbilisi, Georgia

Email : ketinooo@hotmail.com, Email: gurchix@gmail.com

Abstract

The paper deals with reception of solutions for the equation of motion of Poiseuille's laminar flow in magnetic fluids. The different behavior of the magnetic fluid placed into the rotating magnetic field is evident and clear. Here additionally the strong field of the direct, constant current is applied, associated with the growth, and considering the motion of the fluid in the area. The rotating effect of nano-particles in the transversal magnetic field is considered. In MRI of sick fields it represents rather big changes.

Poiseuille's laminar flux flow in an area of a magnetic fluid caused by variations in the pressure along X-axis arrive us to the parabolic shape of the flux, y being the average value for medium and large areas. In the case of mechanical equation of the flux flow [1]

$$-\nabla\vec{p}' + \mu_0\left(\vec{M}\cdot\vec{\nabla}\right)\vec{H} + 2\xi\left(\vec{\nabla}\times\vec{\omega}\right) + (\xi+\eta)\nabla^2\vec{v} = 0. \qquad (1)$$

In the formula (1) x-component has the pressure gradient, the spin-velocity and the term introduced by the viscous flow. We had already received formulae for the spin-velocity as well, as for the density of the momentum [1]

$$-2\xi\frac{\partial v_x}{\partial y} - 4\xi\omega_z + \langle T_{mag,z}\rangle = 0, \qquad (2)$$

deriving this equation and inserting $\partial\omega_z/\partial y$ terms

$$-2\frac{\partial p'}{\partial x}+2\xi\frac{\partial \omega_z}{\partial y}+(\xi+\eta)\frac{\partial^2 \upsilon_x}{\partial y^2}=0, \tag{3}$$

and simplifying these formulae, we get:

$$\frac{\partial \omega_z}{\partial y}=\frac{1}{4\xi}\frac{\partial\langle T_{mag,z}\rangle}{\partial y}-\frac{1}{2}\frac{\partial^2 \upsilon_x}{\partial y^2} \tag{4}$$

and twice integrating the equation (3) by y, we get (appendix 1):

$$-\frac{\partial p'}{\partial x}\frac{y^2}{2}+\frac{1}{2}\int_0^y\langle T_{mag,z}\rangle dy'+\eta\upsilon_x+C_1y+C_2=0, \tag{5}$$

C_1, C_2 being integration constants, while $\langle T_{mag,z}\rangle$ is given as follows:

$$\langle T_{mag,z}\rangle=\frac{1}{2}Re\left(\widehat{m}_x\hat{b}_y^*-\mu_0\left(\hat{h}_x+\widehat{m}_x\right)\widehat{m}_y^*\right). \tag{6}$$

Applying the boundary conditions for υ_x, where y = [0, d], for C_1, C_2 we get:

$$\upsilon_x(0)=0 \quad \text{and} \quad C_2=0 \tag{7}$$

$\upsilon_x(d)=0$ and from it

$$C_1=\frac{d}{2}\frac{\partial p'}{\partial x}-\frac{1}{2d}\int_0^d\langle T_{mag,z}\rangle dy'. \tag{8}$$

Inserting (7) and (9) into (5), we get:

$$v_x = \frac{1}{2\eta}\frac{\partial p'}{\partial x}(y^2 - yd) - \frac{1}{2\eta}\left(\int_0^y \langle T_{mag,z}\rangle dy' - \frac{y}{d}\int_0^d \langle T_{mag,z}\rangle dy'\right). \tag{9}$$

Overwriting the formula (2) in the form of

$$-2\xi\frac{\partial v_x}{\partial y} = \frac{1}{2\xi}\langle T_{mag,z}\rangle - 2\omega_z, \tag{10}$$

and inserting it into the expression for v_x, we receive the value for the spin-velocity ω_z, being independent from v_x,

$$\omega_z = -\frac{1}{4\eta}\frac{\partial p'}{\partial x}(2y - d) + \langle T_{mag,z}\rangle\frac{\eta + \xi}{4\xi\eta} - \frac{1}{4d\eta}\int_0^d \langle T_{mag,z}\rangle dy'. \tag{11}$$

As to the process of reception of the analytical solution of the equation (11) is rather difficult, one may calculate it numerically.

In the easy case, when $\langle T_{mag,z}\rangle$ is too small and may be ignored, for the spin-velocity we have:

$$W_p = -\frac{d^2}{8\eta}\frac{\partial p'}{\partial x}. \tag{12}$$

From it

$$\omega_z|_{y=0} = \omega_z|_{y=d} = \frac{d}{4\eta}\frac{\partial p'}{\partial x} = -\frac{2\,W_p}{d} \tag{13}$$

and the average value of the spin-velocity is zero $\omega_z = 0|_{y=d}$.

Finally the profile of the velocity of Poiseuille's laminar flux flow will be given as follows:

$$v_x(y) = \frac{1}{2\eta}\frac{\partial p'}{\partial x}y(y - d) = \frac{4}{d^2}W_p y(y - d) \tag{14}$$

and the maximal value of W_p at $y = {}^{d}/_{2}$ will be

$$W_p = \upsilon_x\left(\frac{d}{2}\right) = -\frac{d^2}{8\eta}\frac{\partial p'}{\partial x}. \tag{15}$$

Ignoring the flux flow in the area i.e. $\upsilon_x(y) = 0$, we meet the case, when ω_z, $\widehat{m}_x$, $\widehat{m}_y$ and $\langle T_{mag,z}\rangle$ are independent on y, as to ω_z reduces to

$$\omega_z = \langle T_{mag,z}\rangle\frac{\eta+\xi}{4\xi\eta} - \frac{1}{4d\eta}\int_0^d \langle T_{mag,z}\rangle dy' = \frac{1}{4\xi}\langle T_{mag,z}\rangle, \tag{16}$$

$$\omega_z = \frac{1}{8\xi}Re\left(\widehat{m}_x\widehat{b}_y^* - \mu_0\left(\widehat{h}_x + \widehat{m}_x\right)\widehat{m}_y^*\right). \tag{17}$$

Inserting here the values of $\widehat{m}_x$, $\widehat{m}_y$ [2], then the spin-velocity ω_z has the cube solution. In the case of absence of the flux $(\upsilon_x = 0)$, there is dependence of the transversal magnetization of the spin-velocity and the magnetic fluid only on applied transversal magnetic field, where is no any magnetic.

APPENDIX

$$-\frac{\partial p'}{\partial x} + 2\xi\left(\frac{1}{4\xi}\frac{\partial\langle T_{mag,z}\rangle}{\partial y} - \frac{1}{2}\frac{\partial^2\upsilon_x}{\partial y^2}\right) + (\xi+\eta)\frac{\partial^2\upsilon_x}{\partial y^2} = 0, \tag{A}$$

from it

$$-\frac{\partial p'}{\partial x} + \frac{1}{2}\frac{\partial\langle T_{mag,z}\rangle}{\partial y} + \eta\frac{\partial^2\upsilon_x}{\partial y^2} = 0 \tag{B}$$

and it follows

$$-\frac{\partial p'}{\partial x}y+\frac{1}{2}\langle T_{mag,z}\rangle+\eta\frac{\partial \upsilon_x}{\partial y}+C_1=0 \qquad (C)$$

and finally

$$-\frac{\partial p'}{\partial x}\frac{y^2}{2}+\frac{1}{2}\int_0^y\langle T_{mag,z}\rangle dy'+\eta\upsilon_x+C_1y+C_2=0. \qquad (D)$$

REFERENCES

[1] K.V. Kotetishvili, E. Iordanishvili, N. Kobalia, G.G. Chikhladze. Studying the Equation of Motion for Magnetic Fluids with Nano-Particle Inclusions. Journal of Applied Electromagnetism (JAE). Greece. Athens. 2015.

[2] K.V. Kotetishvili, E. Iordanishvili, G.G. Chikhladze. Statement of Boundary Conditions of the Equation for the Magnetic Fluid Including Nano-Particles. Nano Studies. 11. 2015.

[3] Batchelor G.. An Introduction to Fluid Dynamics. Cambridge University Press. 2000.

[4] J. Popplewell, R. Rosensweig et al. Magnetic Field Induced Rotations in Ferrofluids. 26. pp. 1852-1854. 1990.

ON A VISUALIZATION OF LOW FREQUENCY MAGNETIC FIELDS IN MAGNETOTHERAPY (selected from CEMA'15 Conference)

*B. Kudrin, **V. Nikolov

*St. Petersburg State University, Math. & Mech. Faculty,
St.Peterburg, Universitetsky pr. 28
Email: bogdan.kudrin@gmail.com
**Techical University of Sofia
Sofia, bul. Kliment Ohridsky 8
Email: eng.vnikolov@gmail.com

Abstract

In this work we describe a process of visualization of low-frequency magnetic field generated by several coils. The technic was applied to visualize the magnetic field occurring in a special magnetotherapy device — magneto bed. The obtained image shows a patient position, coils, and the magnetic field distribution in the area of coils action. To do this we use 'Paraview' tools, body model and the special scenario – 'Python' language script.

1. INTRODUCTION

It is well known that the calculation and visualization of the low-frequency or constant magnetic field is both a time-and memory consuming. The computation depends on the environment geometry, field influence and the visualization method.

But in the case when we consider the magnetic field generated by a coil (that is the most frequent element in magnetotherapy devices) we can use a mathematical model in which the superposition principle is applied: in this case due to constant current value the induction and self-induction are supposed to be negligible quantities and the common magnetic field is the sum of the fields generated by the contours of a coil. For several coils the resulting magnetic field is the sum over all the coils.

In [1] this problem was solved for 3D case – the magnetic field was calculated in the points of 3D grid. In [2-4] some method for interpolation of magnetic field have been implemented. The visualization algorithms of obtained magnetic field values were discussed in [5,6] and implemented by using Paraview package [7]. The result of the visualization showed the lines of magnetic fields in different ways depending on a selection of Paraview parameters. But such images did not show the patient position.

In this work we consider a visualization method that shows a patient position, coils, and the magnetic field distribution in the area of effect on the patient body. To do this we use Paraview tools, body model and the special scenario – Python language [8] script. Such a scheme allows us to select a pair of coils and corresponding data file (results of calculation or interpolation) and perform the visualization. We also may watch all the pairs step by step. Such a visualization is a practical tool and may considerably help a physician in the estimation of magnetotherapy effects.

2. VISUALIZATION OF MAGNETIC FIELD FOR MAGNETO-BED

We used a system for magneto-therapy called "magnetic bed" (Fig.1). In every moment only one pair of coils is active. In the process of the system functioning every pair of coils is active by turns, and hence a movement of magnetic field occurs. The order of the choice of pairs of coils is defined by a data table recorded in a fle. The numbers of coils and the coordinate system XYZ are shown on the Fig.1.

In previous works we calculated magnetic field generated by a given pair of coils both by mathematical model and the interpolation using experimental data. To visualize the obtained results we use Paraviev package that allows us to show the lines of magnetic field in various regimes.

It should be noted that in the package there are tools to interpolate data for better visualization, in other words Paraview performs an interpolation automatically if necessary.

There is a possibility to show a patient position schematically. For this purpose we use a template from [9] (the file has extension .stl) and Blender package to edit 3D images [10]. To repeat similar actions for different pairs of coils it is convenient to write scenarios (scripts), i.e macros which you may run with given parameter values. Scenario

files are written in Python language and have extension .py. One can write script for a pair of coils or for several ones. We may use a list of coils (where all the pairs and their parameters are given in a definite order) to obtain a script to visualize step by step all the given combinations.

In this work we used results of calculation for the following pairs of coils: (1-5), (1-7), (1-9), (3-11), (1-3), (1-11), (3-7). The obtained data files are numbered in accordance the order in the list of coil pairs. The order of the selection of a result file is given by the user in the script. In our experiments we follow the list of coil pairs, but it may be changed easily.

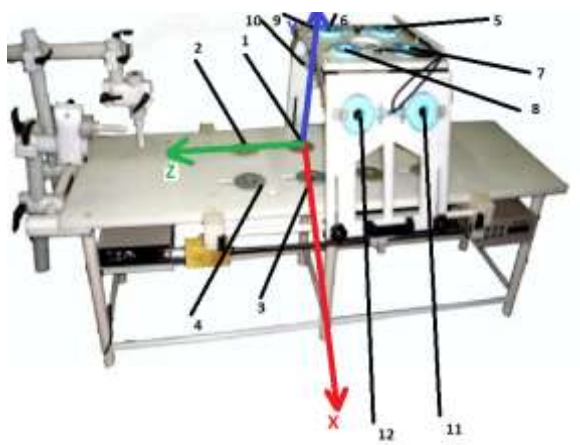

Figure 1. Magneto-bed and the disposition of coils.

3. MAIN STEPS FOR VISUALIZATION

3.1 File loading

To visualize in Paraview the results of calculation (or interpolation by using experimental data) of magnetic field we have to load a data file: File – Open… Select the file required and click the button Apply. Data files have extension .vtk.

3.2 Primitive adding

If we tend to show the position of coils and the bed schematically in accordance with their sizes, we should use so called primitives or primitive objects (cylinder, line, plane, sphere, etc) by performing the following actions:

Find in menu item Sources, select the necessary object and then on the inlay Properties set up its parameters and click button *Apply*.

3.3 Object transformation

To set the primitive in the right position, which in our case is defined from the bed size and the position of the coils in the space we have to perform a transformation. To do it we should select a primitive in Pipeline Browser, then select *Filters – Alphabetical – Transform*. On the inlay Properties set up the parameters and click the button *Apply*

3.4 Resampling

To insert a template in the image (to show a patient body position) we should use a template. After the definition of parameters for primitive objects and the template we can form a final image. It is performed as follows: Select a template (file with extension .stl) in *Pipeline browser*, then select *Filters – Alphabetical – Resample with Dataset*. The file with numerical data should be taken as Input, file of the template as Source. When clicking *Apply* we apply the obtained magnetic field to the template. To set up color scale we use the inlay *Properties* (item *Colors*).

We see that it is very time consuming to repeat the same actions many times. Hence we should write macros (scenario) that describes all necessary steps.

4. HOW TO RUN A SCENARIO

When working we select *Tools – Start Scenario-name*. Then we define the required parameters, perform actions and select *Tools – Stop Scenario-name*.

An example of the scenario written in Python language may be the following. In the text the primitive objects (cylinders that will show the coils) are created. The parameters of the objects are set up in accordance with their sizes in the magneto bed construction. The sign # at the beginning of the string means comment.

```
from paraview.simple import *
import time
#### disable automatic camera reset on 'Show'
```

```
paraview.simple._DisableFirstRenderCameraReset()
# get active view
renderView1 = GetActiveViewOrCreate('RenderView')
# uncomment following to set a specific view size
# renderView1.ViewSize = [808, 783]
# reset view to fit data
renderView1.ResetCamera()
# create a new 'Cylinder'
cylinder1 = Cylinder()
# Properties modified on cylinder1
cylinder1.Height = 34.0
cylinder1.Radius = 58.0
cylinder1.Center = [184.0, 500.0, 116.0]
cylinder1.Capping = 0
# show data in view
cylinder1Display = Show(cylinder1, renderView1)
# trace defaults for the display properties.
cylinder1Display.ColorArrayName = [None, '']
……
# create other cylinders by the same way
……————————————
# create a new 'STL Reader'
body30stl = STLReader(FileNames=['C:\\magneticFieldFiles\\body30.stl'])
# show data in view
body30stlDisplay = Show(body30stl, renderView1)
# trace defaults for the display properties.
body30stlDisplay.ColorArrayName = [None, '']
# create a new 'Transform'
transform1 = Transform(Input=body30stl)
transform1.Transform = 'Transform'
# Properties modified on transform1.Transform
transform1.Transform.Translate = [300.0, 200.0, 1000.0]
transform1.Transform.Rotate = [90.0, 0.0, 0.0]
transform1.Transform.Scale = [200.0, 200.0, 200.0]
# show data in view
transform1Display = Show(transform1, renderView1)
# trace defaults for the display properties.
```

```
transform1Display.ColorArrayName = [None, '']
```

5. VISUALIZATION ALGORITHM AND EXAMPLES

The visualization algorithm may be the following.

- Calculate magnetic field induction for given pairs of coils. Number the obtained files in accordance with the list of coil pairs.
- Put in a working directory obtained data files, file containing 3D model of a body (template) and script file. In the script file the path to the working directory is given.
- Load script in Paraview and run it. When script running we see the picture of magnetic field distribution.
- Save screenshots by using Paraview tools
- Stop script running.

The block scheme of the algorithm is the following.

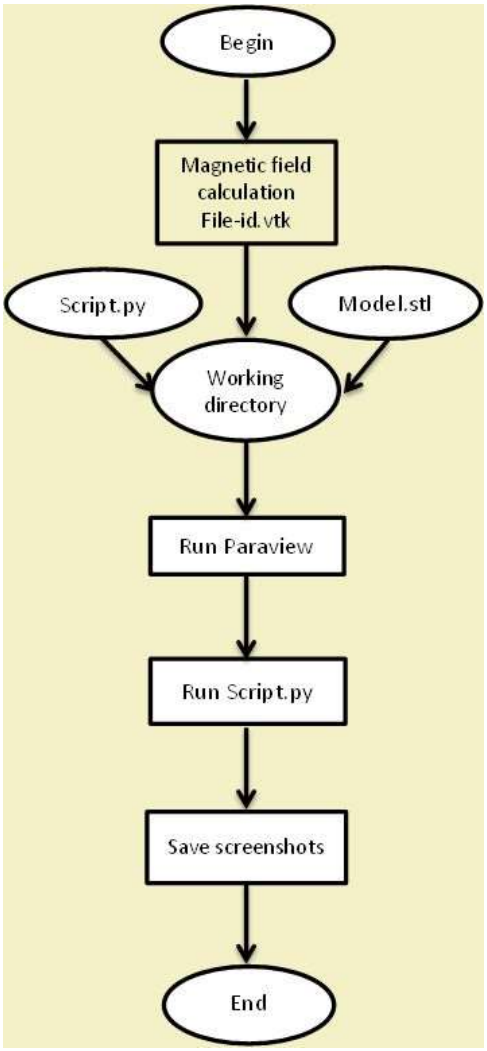

Figure 2. Block scheme of the visualization algorithm for the configuration of magneto bed coils.

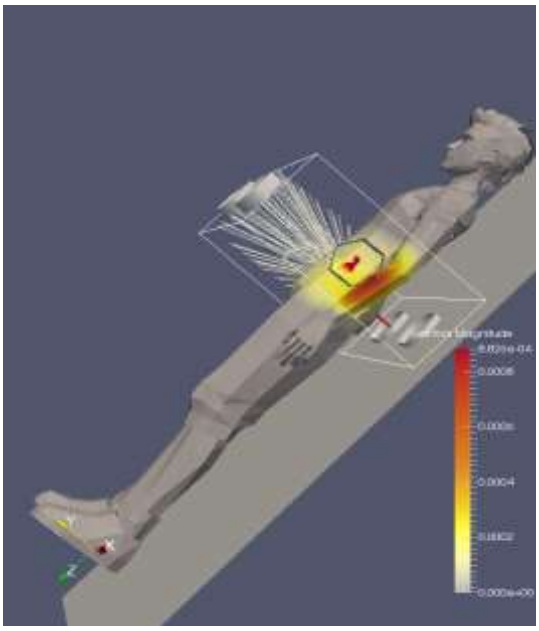

Figure 3. Visualization results for the pair of out-of-line coils.

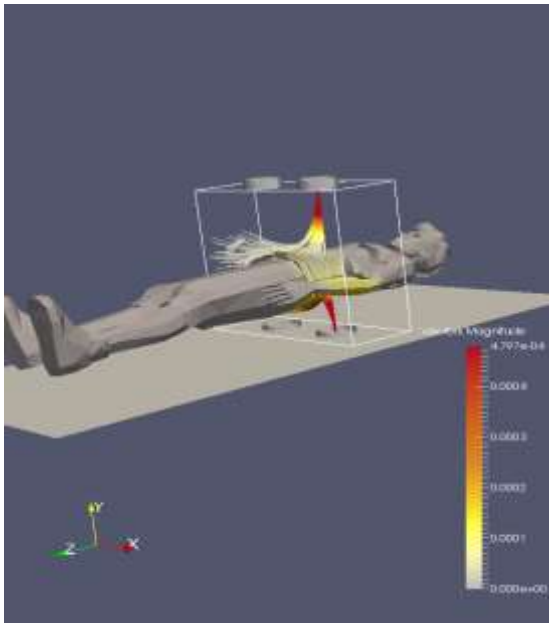

Figure 4. Visualization results for the pair of coaxial coils.

6. CONCLUSION

The implemented technic allows us to visualize the numerical data obtained by the calculation or interpolation of low-frequency magnetic field such that the position of a patient and the coils are shown. We use freeware packages Paraview and Blender, and

templates for 3D images. To optimize the process of showing we use the Python language script. All the calculation may be performed before the visualization. The described method may be used for any magnetotherapy device.

ACKNOWLEDGEMENT

The work was partially supported by RFBR grant 13-01-00782.

REFERENCES

[1] N. Ampilova, D. Dimitrov, B.Kudrin. Mathematical modeling of low frequency magnetic field in systems for magnetotherapy . Proc. 8 Int. Conf. CEMA13, 17-19 Oct. 2013, Sofia, Bulgaria. p.48-51.

[2] B.Kudrin, I.Soloviev. On interpolation methods of low frequency magnetic field in systems for magnetotherapy. Proc. 9 Int. Conf. CEMA14, 16-18 Oct. 2014, Sofia, Bulgaria. KING 2001, p.154-157. ISSN 1314-2100.

[3] B.Kudrin,V.Nikolov. Algorithms of interpolation and visualization of low frequency magnetic field using experimental data. Proc. 9 Int. Conf. CEMA14, 16-18 Oct. 2014, Sofia, Bulgaria. KING 2001, p.43-45. ISSN 1314-2100.

[4] B.Kudrin,V.Nikolov. On the mathematical model of interpolation of low frequency magnetic field using experimental data. Proc. 9 Int. Conf. CEMA14, 16-18 Oct. 2014, Sofia, Bulgaria. KING 2001, p.80-84. ISSN 1314-2100.

[5] B.Kudrin, A.Dimitrov. An algorithm for visualization of low-frequency magnetic signals in systems for magnetotherapy. Proc. 8 Int. Conf. CEMA13, 17-19 Oct. 2013, Sofia, Bulgaria. p.31-35.

[6] B.Kudrin, A.Dimitrov. Computer visualization of low-frequency magnetic signals in systems for magnetotherapy with variable parameters. Proc. 8 Int. Conf. CEMA13, 17-19 Oct. 2013, Sofia, Bulgaria. p.36-39.

[7] ParaView Tutorial: http://paraview.org/Wiki/images/d/d5/ParaViewTutorial398.pdf

[8] Python programming language: http://www.docs.python.org

[9] http://tf3dm.com/3d-model/boy-10833.html

[10] https://www.blender.org/

EMG DRIVEN ACTIVE PROSTHESIS : SIGNAL ACQUISITION SYSTEM DESIGN AND INITIAL EXPERIMENTAL STUDY (selected from CEMA'15 Conference)

D. Dimitrov, V. A. Nedialkov, K. Dimitrov

Department of Radio Communication and Video Technologies, Faculty of Telecomunications, Technical University of Sofia, 8 Kl. Ohridski Blvd, Sofia

Email: dcd@tu-sofia.bg, Email: viktor@alned.com

Abstract

A multi-channel EMG amplifier and acquisition system is proposed. The system is composed of portable signal amplifier and dedicated real-time signal processing software. The system is intended to be used with myoelectric prostheses, therefore there is an emphasis on the multichannel real-time acquisition, portability, current consumption and connectivity features. The goal of the design is to implement the latest low-power high speed technologies available on the market today and also the system is intended to test EMG signal processing algorithms. This document covers the EMG signal all the way from the muscle through the amplifier, the Driven Right Leg (DRL) noise suppressor, filtering, digitalization, PC communication, the signal processing algorithm and the real-time visualization of the results. The article includes complete schematics, analysis and tests of the device.

1. INTRODUCTION

In individuals who have lost limbs, in order to recreate the movement of the limb with an active prosthesis, an estimation must be made based on other muscles used for particular movement. A detailed study must be performed to record the muscles activity in healthy individuals.

First we need to understand the biomechanics of human walking, as this information plays a crucial role in the design of such systems. A simplified diagram of human walking gait is shown on Fig.1 [1], [9]

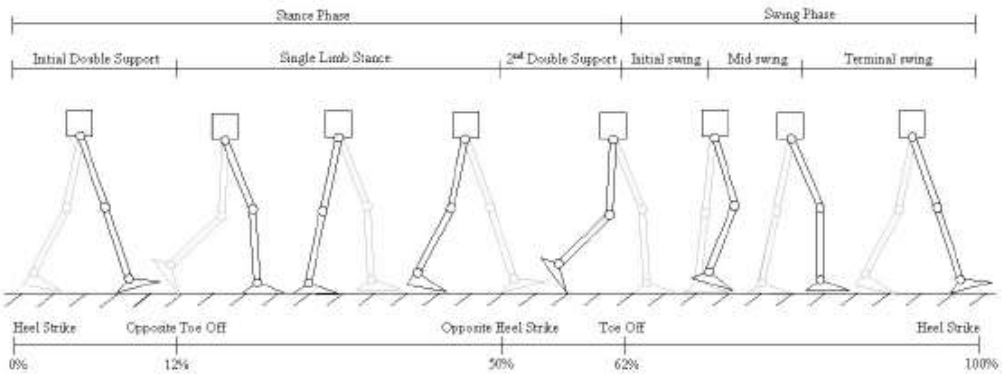

Figure 1. The human gait

Note that the timing of the labelled events during the gait cycle is approximate, and varies across individuals and conditions. The human walking gait cycle is typically represented as starting (0%) and ending (100%) at the point of heel strike on the same foot, with heel strike on the adjacent foot occurring at approximately 62 % of gait cycle.

In general, the human leg can be thought of as a seven degrees of freedom structure, with three rotational degrees of freedom at the hip, one at the knee and three at the ankle. A description of the human anatomical planes as well as a kinematic model of the human leg in the sagittal plane, which is the dominant plane of motion during human locomotion.

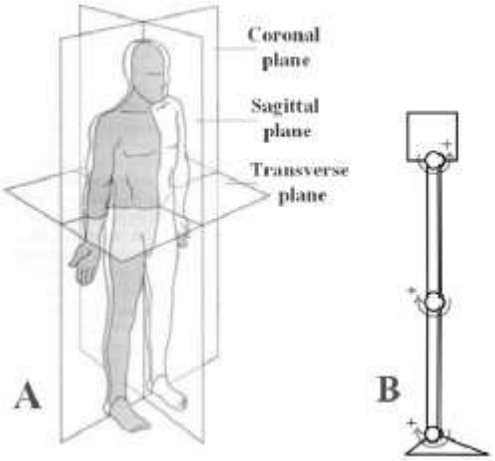

Figure 2. The human planes

Skeletal muscle is organized functionally on the basis of the motor unit (fig. 3). The motor unit is the smallest unit that can be activated by a volitional effort, in which case all constituent muscle fibres are activated synchronously. The component fibres of

the motor units extend lengthwise in loose bundles along the muscle. In cross section, however the fibres of a given motor unit are interspersed with fibres of other motor units. Thus the component muscle fibres of the single motor unit (SMU) constitute a distributed, unit bioelectric source located in a volume conductor consisting of all other muscle fibres, both active and inactive. [2]

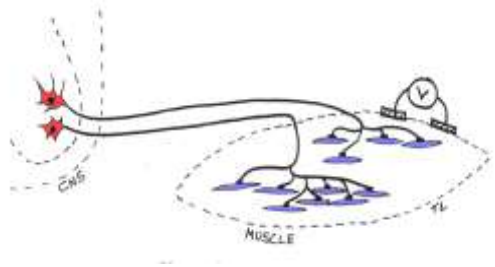

Figure 3. The Motor Unit

The evoked extracellular field potential from the active fibres of an SMU has a triphasic form of brief duration (3-15ms) and an amplitude of 20-2000 uV, [3] (fig 2) depending on the size of the motor unit. Due to the small size of the SMU the recording of the SMU action potential is only possible with needle electrodes. When using surface electrodes the recorded signal consists of many SMU action potentials form different depths. The resultant signal has a frequency range from 25Hz to several thousand Hertz and amplitude in the range of of 20-2000 uV (fig. 3)

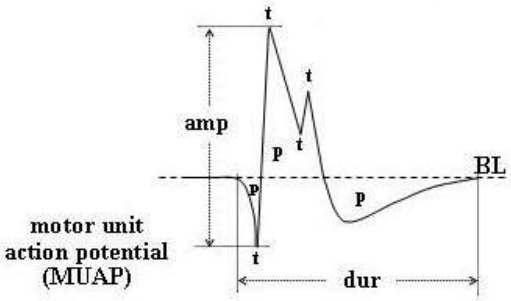

Figure 4. Motor unit action potential

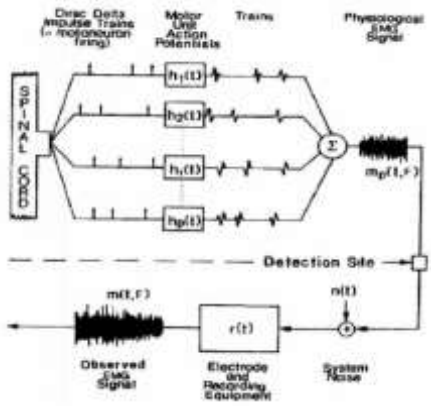

Figure 5. The EMG resultant signal

2. THE RECORDER

The amplifier must be designed to cover this frequencies and amplitudes.

According to Nyquist-Shannon theorem, which basically says that the sampling frequency must be at least two times higher the then the highest frequency sampled. If this theorem is not respected, aliasing will occur. The above requirement has important consequences to the design because we must choose a cutoff frequency high enough not to lose valuable signal but low enough to avoid a very complicated and expensive design.

The core of the design is the microcontroller. It must be chosen very carefully so that it is powerful enough to be able to process the data at the chosen sampling rate but at the same time to be with as low as possible current consumption. High power consumption will need bigger batteries hence the design will became bigger and heavier.

There are several communication possibilities for the design. In recent years many manufactures developed small and easy to implement OEM modules for different type of communication – USB, Wireless, Bluetooth and GSM modules. For this design a Bluetooth module is chosen because, we need a wireless communication with enough speed and a distance no more then 10-20 meters, which is perfectly covered by the Bluetooth module.

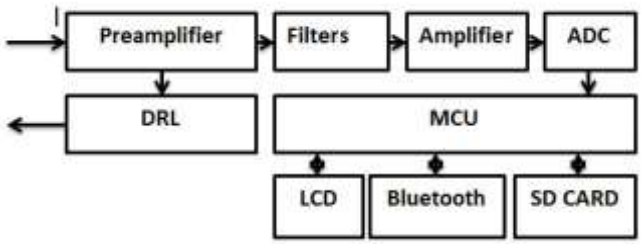

Figure 6. Block diagram of the recorder.

2. 1. Amplifier

A three-channel amplifier has been designed to measure the EMG signal. The block diagram depicted in Figure 6 shows the different stages. The amplifier consists of: preamplifier, Driven Right Leg (DRL), filter, second amplification stage.

2.1.1 Preamplifier

The preamplifier is based on the AD627 instrumentation amplifier by Analog Devices. This IC has very good CMRR, very low offset voltage, and very high input impedance. Also it is a micro-power and has rail to rail operation which can allow us to use lower voltage levels.

The gain of the amplifier is determined by the formula:

$$\text{Gain}= 5+(200\text{k}\Omega/\text{Rg})$$

$$\text{Rg}=200\text{k}\Omega/(\text{Gain}/5)$$

A gain of 10 have been chosen for this stage.

A group of resistor and diodes clamped to the supply rails is used to protect the inputs from static discharge. The resistor and the 56 pF capacitor form low-pass stability filter.

During testing of the initial device a problem was discovered. Due to the very high input impedance of the AD627, when an electrode inadvertently falls the amplifier saturates in all channels through the DLR schematic. To solve this problem and to assure redundancy of the system TLC 2252 micro-power opamps were added before the instrumentation amplifier as a simple voltage follower.

2.1.2 Driven Right Leg (DRL)

The biggest noise origin in the EMG bandwidth is the electrical network interference. It produces a common mode voltage in the patient body and sometimes this voltage is higher than the useful signal. The DRL system is based on a feedback circuit that drives the common-mode voltage back to the patient body, amplified and phase reversed by 180°. This feedback improves the CMRR by an amount equal to (1+A) where A is the closed loop gain of the feedback loop.

In this design the common voltage is collected by from the two resistors of the Rg group. Then through a voltage follower, which purpose is to protect the gain circuitry, it goes through an inverting amplifier which reverses it to 180°. And then it goes back to the patient. A current limiting resistor is added to protect the patient. A typical DRL implementation is shown on fig. 7 [4].

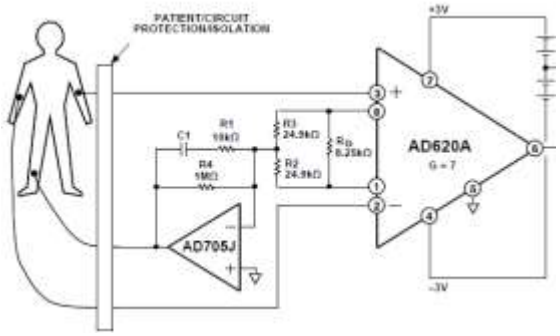

Figure 7. Driven Right Leg.

2.1.3 Filters

After the preamplifier the next stage is the groups of high-pass and low pass filters. The frequency range of the amplifier is chosen to be 25Hz – 500Hz. This range is chosen to eliminate the low frequency noise witch is mostly below 25Hz. The upper cutoff frequency is chosen so that the signal will include the most of the EMG signal and to ease the signal processing.

Simple RC filters are chosen for this stage. First it is the high-pass filter and then the low pass.

$$Fc=1/2\pi RC$$

For High Pass we have:

C=0.22uF and R=33kΩ Fc=22Hz

For Low pass we have:

C=0.056uF and R=5.6kΩ Fc=507 Hz

2.1.4 Second Stage Amplifier

The second stage amplifier is a non-inverting amplifier with a gain of 50. In this stage we translate the signal to single-supply with a zero-point at 1.65V. MCP609 is used for the design. It is a micro-power rail to rail op-amp, designed for single-supply purposes. Additional filtering is added at the gain setting network and at the output of the amplifier.

2.1.5 ADC

A dedicated multichannel ADC - ADS7844 schematic is used. It is a micro-power 8-channel ADC with SPI communication. The maximum sampling rate is 200kHz.

Most of the present day microcontrollers have ADC integrated into them by using them instead of a dedicated ADC presents several problems. First it is the power supply decoupling. To improve the noise suppression usually the power lines in the analog schematic is decoupled through a LC network to supress the noise from the digital schematics. Using the MCU ADC will add noise to the analog schematic.

Another problem is design commonality. If we change the microcontroller we need to redesign also the analog part of the schematic to use the new MCU ADC.

Since the upper frequency of the amplifier is set to 500Hz and according to the Nyquist-Shannon theorem, the minimum sampling rate per channel is 1000Hz. To further improve the digitalization a sampling rate of 2000Hz is chosen. The amplitude range of the signal is from 0V to 3.3V

The general parameters of the amplifier are:

- Frequency response: 25Hz-500Hz
- Total Gain: 500

- Dynamic range: ±3.3 mV

2.2 Digital part

The digital part of the device consists of: MCU , LCD for displaying critical data, the Bluetooth transceiver and a SD card holder for logging data.

2.2.1 Microcontroller

There is a wide variety of options for the Microcontroller. The chosen MCU for this project is the Microchip PIC24FJ128A306 [5]. It is a 16-bit MCU with 128kB of Program memory, 8KB of RAM, NanoWatt Technology for extreme low power consumption and up to 32MHz of operation speed.

The main reason to choose this MCU for the project are

- The very low power consumption
- High speed
- Low profile
- The availability of the Peripheral Pin Select function
- The available Development tools MPLAB and MICROCHIP C16 C-compiler

2.2.2 Bluetooth transceiver

Bluetooth was chosen for the design. It will give freedom of movements for the device and has enough range. There are many manufacturers of Bluetooth transceivers, which function as a simple serial port over Bluetooth. There is no need to develop specialized applications and drivers for communications, because it is transparent to the MCU and the host computer. Based on popularity and known quality the SENA PARANI BCD-210 was chosen [6]. The module is first configured with the tool ParaniWin where the speed and authentication options are set.

Figure 8. Parani BCD210DC.

3. SIGNAL PROCESSING SOFTWARE

The function of the software is to perform the signal processing and data visualization in real-time.

3.1. EMG signal processing algorithm

The most frequently used algorithms for detecting muscle contraction consists of simple integration of the EMG signal. This is simple enough and can be implemented even with hardware means only, but does not provide enough sensitivity and signal to noise separation.

Pan and Tomkins [7] have proposed a real-time algorithm for detection of the ECG QRS complex based on analysis of the slope, amplitude and width of QRS complexes. The algorithm includes a series of filters and methods that perform low-pass, high-pass, derivative, squaring, integration, adaptive thresholding, and search procedures. Figure 9. Illustrates the steps of the algorithm in schematic form.

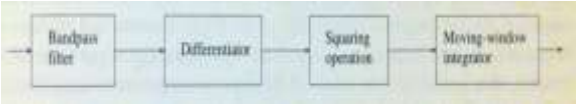

Figure 9.

The band-pass filter eliminates the noise from electrical interference and the low-frequency noise (baseline drift, P and T wave). The derivative operator further suppresses the low frequency components of the P and T wave and motion artifacts and provide large gain on the high-frequency components. The squaring makes the result positive and further emphasize high-frequency components. The subsequent moving average

integration smooth the multiple peaks within the duration of a single QRS complex. The a set of thresholds are calculated for the signal and the noise.[3] A result of the Pan and Tompkins algorithms is shown on figure 10.

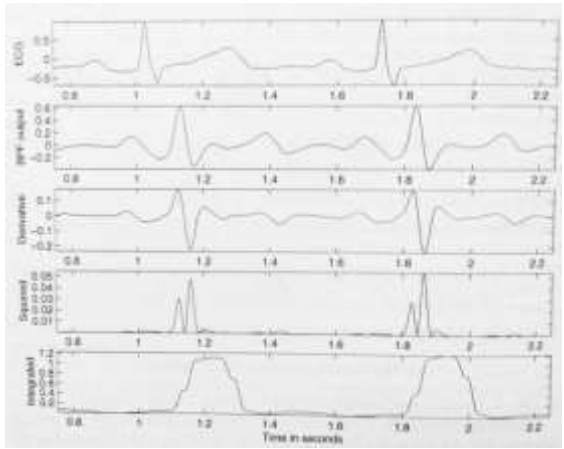

Figure 10.

The use of Pan-Tompkins algorithm was inspired by the insight that the EMG signal can be very random and depends on the MUPs activated, the place and size of the surface electrodes used. This is why a pattern recognition is very difficult and not reliable enough. On the other hand this algorithm is very sensitive to the power of the signal witch is directly related to the strength of contraction.

The low-pass and high pass-filters used in the original Pan-Tomkins algorithm are omitted because in the frequency band of the digitized signal the low-frequency and high frequency noise is already filtered.

The steps used in the algorithm are the following:

- Derivative operator: The derivative operation used is specified as:

$$y(n)=1/8[2x(n)+x(n-1)-x(n-3)-2x(n-4)]$$

- Squaring: $y(n)^2$ - this makes the result positive and emphasizes the large differences
- Moving average: The moving average smooth the multiple peaks from the squaring operation:

$$y(n)=1/N[x(n-(N-1))+x(n-(N-2))++x(n)]$$

The window width is chosen to be N=500 in the proposed algorithm.

- Adaptive thresholds: In this step it is important to find accurately the onset and the offset of the muscle contraction. Since the muscle can by contracted slowly or very rapidly a slope analysis is not suitable. Therefore only amplitude threshold is used which is defined as:

$$THR = 0.1*MAX_CONTRACTION$$

3.2. Visualization

The discretisation frequency is 2000Hz and the serial port data pooling is set at 2ms. The calculation stage is performed for every data element of the signal. The screen calculation is also made for every data element but it is not possible to draw directly to the screen with 2000Hz draw frequency. That is why the process of visualization is divided into two stages – Draw to memory and copying of the memory buffer to the screen at a reasonable frequency.

We first create the memory screen buffers:

```
m_pMemDC->CreateCompatibleDC(pDC);
m_pBitmap->CreateCompatibleBitmap (pDC ,ClientRect.right,ClientRect.bottom);
```

Another buffer is also used for the raster of the screen. A timer is started with a period of 20 ms. Every time an event is triggered the event handling function executes a copy of the memory buffer to the screen.

```
m_pMemDC->BitBlt(ClientRect.left,
ClientRect.top,ClientRect.right,ClientRect.bottom,m_pMemDCRaster,0,0,SRCAND);
pDC->BitBlt(ClientRect.left,
ClientRect.top,ClientRect.right,ClientRect.bottom,m_pMemDC,0,0,SRCCOPY);
```

The first line copies the screen raster to the memory buffer and the second line copies the memory buffer to the screen.

4. EXPERIMENTS

The results from the EMG signal processing algorithm are shown on fig.11. On the first line is the raw signal, below it is the derivative, then the squared signal and finally the result from the moving average.

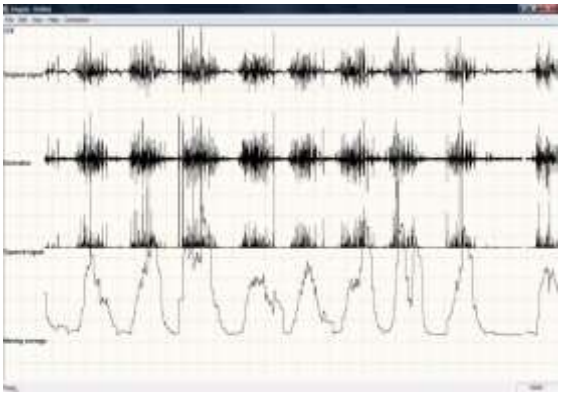

Figure 11. Rectus femoris during walking.

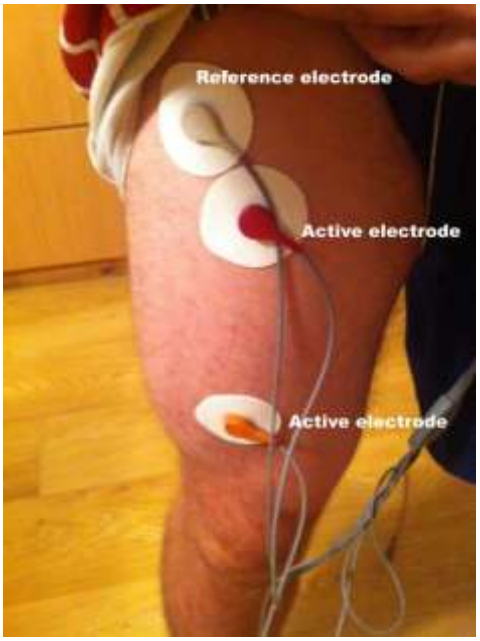

Figure 12. Electrode placement for the Rectus femoris experiment.

First we examine the EMG signals during normal walking. We put the electrodes of the first channel on the rectus femoris and the second channel on the biceps femoris (Fig 13).

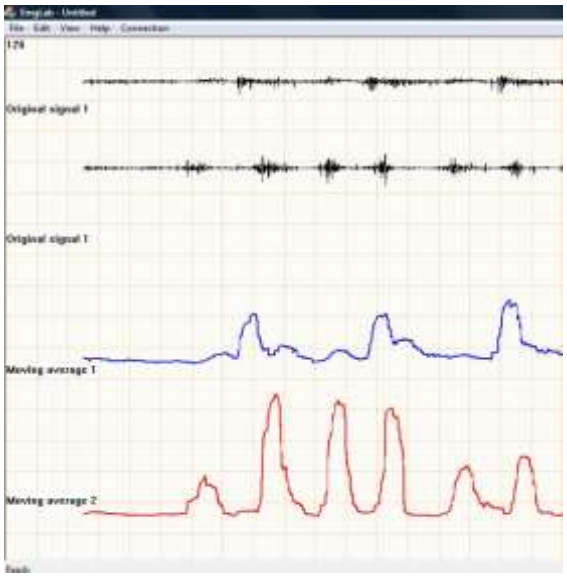

Figure 13. Normal walking.

In the moving average results of the signal we see that first we have a contraction of the biceps femoris then a contraction of the rectus femoris, followed by another contraction of the biceps femoris. The first contraction of the biceps femoris is the lifting of the lower leg of the ground, then the rectus femoris swing the leg forward and then the biceps femoris again takes the load of the bodyweight[8].

The second experiment is a step climb. Again the electrodes are above rectus femoris and biceps femoris (Fig. 14).

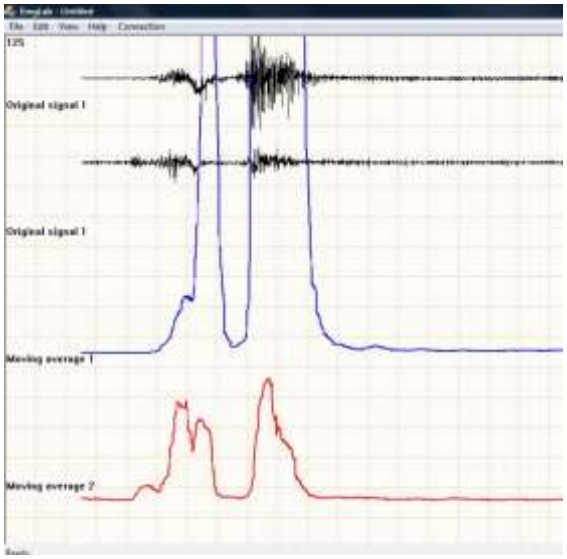

Figure 14. Step climb.

Here we have a double amplitude peak signal in both muscles which are synchronous. The first impuls is shorter and is associated with the lifting of the leg and planting it on the step, while the second one is the lifting of the body by the leg.

The third experiment is the stepping down motion. Electrodes are again on the rectus femoris and biceps femoris (Fig. 15).

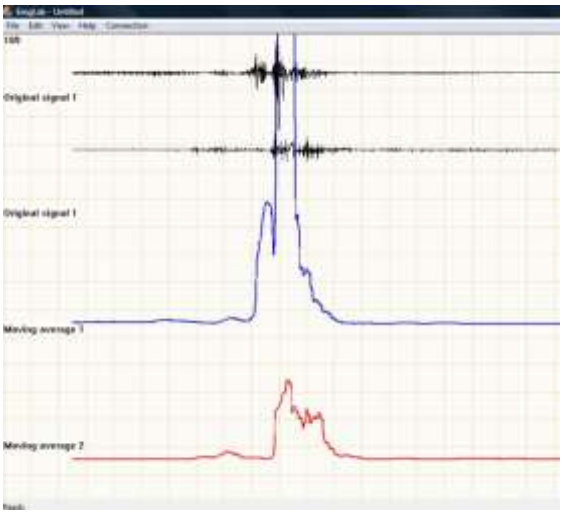

Figure 15. Step down.

We have again synchronous signals from both muscles but the signal from rectus femoris is much bigger and is two-phase. The first phase corresponds to the lifting of the leg while the second much bigger phase begins with the planting of the leg on the ground and the beginning of taking the load on it.

5. CONCLUSION

The recorder extracts very well the EMG signals from the muscles. The light weight and small size make it transparent the test patient, which gives us very accurate experimental results for the patients gait and movements. The algorithm gives very good results on the detection of the muscle contraction of different muscles. During walking the work of the muscle visible and the onset and offset of the contraction can easily be detected. Further experiments are needed to tune the size of the Moving Average N.

We were able to obtain signals from the most common movements – walking, climbing and stepping down. With the Software Emg Lab we were able to record the behaviour of the muscles during this exercises.

From the results obtained we can clearly distinguish all types of movements from just two muscles – rectus femoris and biceps femoris. This can allow us to control the knee joint with a certain degree of accuracy.

Further development may include adding more channels to monitor other channels. Also a study needs to be performed to find a relationship between the movement of the above the knee muscles and the ankle joint.

REFERENCES

[1] J. Rose and J.G. Gamble, Human Walking, Williams and Wilkins, Baltimore, MD, USA, 2nd ed., 1994.

[2] Webster J, "Medical Instrumentation – application and design" John Wiley & Son

[3] Rangaraj M. Rangayyan "Biomedical Signal Analysis" Wiley – Interscience

[4] Analog Devices AD620 Datasheet - http://www.analog.com/en/products/amplifiers/instrumentation-amplifiers/ad620.html

[5] MICROCHIP PIC24FJ128GA306 Datasheet – http://www.microchip.com/wwwproducts/Devices.aspx?product=PIC24FJ128GA306

[6] Sena Industrial Parani BCD210 Datasheet, http://www.senaindustrial.com/products/industrial_bluetooth/bcd210.php

[7] Pan J and TompkinsWJ. "A real-time QRS detection algorithm." IEEE Transaction on Biomedical Engineering, 32:230-236, 1985

[8] Boundless. "Muscles that Cause Movement at the Knee Joint." Boundless Anatomy and Physiology. Boundless, 21 Jul. 2015. https://www.boundless.com/physiology/textbooks/boundless-anatomy-and-physiology-textbook/the-muscular-system-10/muscles-of-the-lower-limb-107/muscles-that-cause-movement-at-the-knee-joint-579-9335/

[9] Aaron M. Dollar and Hugh Herr "Active Orthoses for the Lower-Limbs: Challenges and State of the Art" Proceedings of the 2007 IEEE 10th International Conference on Rehabilitation Robotics, June 12-15, Noordwijk, The Netherlands.